Available online at www.sciencedirect.com
ScienceDirect
Journal of Computational Physics 219 (2006) 671–696
JOURNAL OF COMPUTATIONAL PHYSICS
www.elsevier.com/locate/jcp

Strongly coupled flow/structure interactions with a geometrically conservative ALE scheme on general hybrid meshes

Hyung Taek Ahn *, Yannis Kallinderis

Institute for Computational Engineering and Sciences, The University of Texas at Austin, 1 University Station, C0200, Austin, TX 78712, USA

Received 25 September 2005; received in revised form 7 April 2006; accepted 10 April 2006
Available online 12 June 2006

Abstract

A geometrically conservative finite-volume arbitrary Lagrangian–Eulerian (ALE) scheme is presented with general hybrid meshes. A moving mesh source term is derived from the geometric conservation law and physical conservation laws on arbitrarily moving meshes. The significance and effectiveness of the moving mesh source term regarding uniform flow preservation is demonstrated and also compared to a different ALE formulation without such a source term. The temporal accuracy of the current ALE scheme does not deteriorate with the use of moving meshes. The applicability of the presented ALE scheme is demonstrated by simulating vortex-induced vibrations (VIV) of a cylinder. Two different flow–structure coupling strategies, namely weak and strong, are employed and compared. The proposed strong coupling is implemented with a predictor–corrector method, and its superior stability and time accuracy over weak coupling schemes is demonstrated. The present scheme can employ general hybrid meshes consisting of four different types of elements (hexahedra, prisms, tetrahedra and pyramids) and yields good agreement with other computational and experimental results.

Keywords: Flow/structure interaction; Vortex-induced vibration; Strong coupling; Arbitrary Lagrangian–Eulerian scheme; Geometric conservation law; General hybrid meshes

1. Introduction

Moving mesh problems in computational fluid dynamics (CFD) have become of great interest due to their wide area of applications. Blood flow through the arteries of the human heart, aircraft wing flutter, free surface flows, parachute inflation, airbag explosion and several other kinds of flow–structure interaction problems can be classified in this category.

In order to simulate the fluid dynamics problem with moving mesh and boundaries, several approaches have been proposed, such as the arbitrary Lagrangian–Eulerian (ALE) scheme [1], the space–time approach [2,3], and the immersed boundary method [4–6].

* Corresponding author.
E-mail addresses: ahn@mail.utexas.edu (H.T. Ahn), kallind@veltisto.net (Y. Kallinderis).

0021-9991/$ - see front matter
doi:10.1016/j.jcp.2006.04.011

The ALE formulation is based on the description of the flow field on a moving frame of reference which is typically attached to the moving surface(s). It was originally introduced in the finite-difference frame work by Hirt et al. [1] with structured meshes. The ALE scheme with the finite-difference method has been successfully extended to arbitrarily polygonal meshes by Shashkov and his collaborators [7,8]. The ALE scheme was also adopted by the finite-element community by Hughes [9–11]. In the finite-volume community, the ALE scheme is actively used in aerodynamic applications [12–16] for compressible flows, such as aeroelasticity and wing flutter analysis.

In the ALE finite-volume method, the mesh follows the motion of the interface between the fluid and solid boundary. Hence, the mesh velocity appears in the convective flux term of the formulation. The space–time approach is based on a finite-element formulation of the governing equations which is written over a sequence of space–time slabs. In this formulation, the finite-element interpolation polynomials are functions of both space and time. Lastly, in the immersed boundary method, a body in the flow field is considered as a kind of momentum forcing term in the Navier–Stokes equations rather than a real body. In this method, the choice of accurate interpolation schemes satisfying the no-slip condition on the immersed body is crucial because the mesh does not generally follow the immersed body boundary. Among all three approaches, the ALE scheme is the most popular method in the CFD community and has been chosen for the current study.

For the stable and accurate simulation on moving meshes, the time integration scheme should be developed such that it preserves its stability and accuracy of its fixed mesh counterpart. Furthermore, the motion of the mesh should not deteriorate the stability, accuracy, and the preservation of uniform flow.

In the development of stable and accurate time integrators for ALE schemes and identification of the role of the geometric conservation law (GCL) in terms of accuracy and stability, there have been considerable research efforts, especially by Farhat's group and their collaborators [12–15]. Essentially, the ALE time integration schemes developed by Farhat are based on either time-averaging of the fluxes evaluated on different mesh configurations, or on evaluation of the fluxes on a time-averaged mesh configuration [16]. Such schemes offer second order of accuracy in time with obeying of the GCL property, but the time-averaging process among the multiple mesh configurations can be a demanding task in terms of computational and/or memory requirement.

A different approach followed by others is the ALE formulation with a moving mesh source term [17–19]. Even though such a formulation has produced reasonable results in moving mesh simulations, there was neither a clear derivation of the source term, nor detailed discussion of its significance. To be sure about the validity of the ALE formulation with moving mesh source term, we have to be able to derive the moving mesh source term from the original conservation laws, and address its significance in moving mesh simulations.

One aspect of the present work is the derivation and validation of the ALE scheme with a moving mesh source term, and the other is its application to flow and structure interaction problems involving mesh motion. For the coupling of the flow and structural solvers, two different strategies can be employed, namely strong and weak coupling. For the present study, the strong coupling is based on the predictor–corrector method. Its superior stability is demonstrated via comparisons with the corresponding weak coupling scheme. The developed method is mesh-topology independent and its use with general hybrid meshes consisting of hexahedra, prisms, tetrahedra and pyramids is also presented.

In the first part of the present study, we derive the ALE formulation with a moving mesh source term from the physical conservation laws and geometric conservation law. Then, we present the significance of the moving mesh source term on preservation of uniform flow solution with arbitrarily deforming meshes. The result of the current ALE formulation with the moving mesh source term is compared to that of a different ALE formulation which does not include such a source term. A time step refinement study is performed and the order of accuracy is confirmed on moving mesh configurations via comparisons with a reference solution.

In the second part, the ALE scheme is applied to the vortex-induced vibration (VIV) of a flexible cylinder. A single degree-of-freedom model of a two-dimensional cylinder is extended to three dimensions. Beam elements are used to model the flexural vibration of the cylinder in three dimensions, and then the equation of motion for the cylinder is normalized by using the same reference quantities as those used for normalization of the flow governing equations. The superior stability of strong coupling over weak coupling is emphasized

via comparison between the two coupling methods employing cases of vortex-induced vibration of the cylinder. The present computational results are compared with other computational and experimental results in both two and three dimensions.

2. Finite volume ALE formulation with the method of artificial compressibility

The incompressible Navier–Stokes equations in arbitrary Lagrangian–Eulerian (ALE) frame are derived from the conservation laws for an arbitrarily moving control volume. The moving mesh source term is obtained from the integral form of the conservation laws, and its relation to the geometric conservation law (GCL) is addressed. The governing equations are normalized by using free stream flow properties and a characteristic length scale. A time-accurate artificial compressibility method is introduced for the unsteady simulation of incompressible viscous flow.

2.1. Governing equations

The conservation laws of mass and momentum for an arbitrarily moving control volume $V(t)$ with boundary $S(t)$ can be expressed in integral form as follows:

$$\frac{\mathrm{d}}{\mathrm{d}t}\int_{V(t)}\rho\,\mathrm{d}V+\oint_{S(t)}\rho(\mathbf{V}-\mathbf{V}_\mathrm{b})\cdot\hat{\mathbf{n}}\,\mathrm{d}S=0, \tag{1}$$

$$\frac{\mathrm{d}}{\mathrm{d}t}\int_{V(t)}\rho\mathbf{V}\,\mathrm{d}V+\oint_{S(t)}\rho\mathbf{V}(\mathbf{V}-\mathbf{V}_\mathrm{b})\cdot\hat{\mathbf{n}}\,\mathrm{d}S=\oint_{S(t)}\sigma\cdot\hat{\mathbf{n}}\,\mathrm{d}S+\int_{V(t)}\rho\mathbf{f}\,\mathrm{d}V, \tag{2}$$

where $\mathbf{V}$ is the flow velocity and $\mathbf{V}_\mathrm{b}$ is the control volume boundary velocity. If $\mathbf{V}$ is equal to $\mathbf{V}_\mathrm{b}$, then the flux term vanishes and the formulation is identical to the one in a Lagrangian frame of reference. If $\mathbf{V}_\mathrm{b}=0$, then the control volume is fixed in space and the formulation corresponds to the one in an Eulerian frame of reference.

The two terms on the right-hand side of Eq. (2) are the external forces acting on the control volume. The first term is the surface force acting on the boundary of the control volume, and the second term is the body force which is neglected here. The stress tensor σ is composed of the normal stresses representing hydrostatic pressure, and shear stress parts

$$\sigma_{ij}=-p\delta_{ij}+\tau_{ij}.$$

For a Newtonian fluid under incompressible flow condition, the shear stress tensor is expressed as

$$\tau_{ij}=\mu\left(\frac{\partial u_i}{\partial x_j}+\frac{\partial u_j}{\partial x_i}\right).$$

The equations are normalized by using the following relations to the reference quantities:

$$x^*=\frac{x}{D},\quad u^*=\frac{u}{U_\infty},\quad t^*=\frac{t}{D/U_\infty},\quad p^*=\frac{p-p_\infty}{\rho U_\infty^2},$$

where D is the characteristic length scale which is the diameter of the circular cylinder, U_∞ is the free stream velocity, and p_∞ is the free stream pressure. Substituting the above relations into the conservation laws and dropping the symbol $*$ yields the normalized form of the governing equations. The incompressible Navier–Stokes system, which consists of the continuity and three momentum equations, one for each coordinate direction, is expressed in the following integral form:

$$\frac{\mathrm{d}}{\mathrm{d}t}\int_{V(t)}\mathbf{U}\,\mathrm{d}V+\oint_{S(t)}\left(\mathbf{F}_\mathrm{I}\hat{\mathbf{i}}+\mathbf{G}_\mathrm{I}\hat{\mathbf{j}}+\mathbf{H}_\mathrm{I}\hat{\mathbf{k}}\right)\cdot\hat{\mathbf{n}}\,\mathrm{d}S=\oint_{S(t)}\left(\mathbf{F}_\mathrm{V}\hat{\mathbf{i}}+\mathbf{G}_\mathrm{V}\hat{\mathbf{j}}+\mathbf{H}_\mathrm{V}\hat{\mathbf{k}}\right)\cdot\hat{\mathbf{n}}\,\mathrm{d}S, \tag{3}$$

where $\mathbf{U}$ is the vector of conserved flow properties, $\mathbf{F}_\mathrm{I}\hat{\mathbf{i}}+\mathbf{G}_\mathrm{I}\hat{\mathbf{j}}+\mathbf{H}_\mathrm{I}\hat{\mathbf{k}}$ is the convective flux vector, $\mathbf{F}_\mathrm{V}\hat{\mathbf{i}}+\mathbf{G}_\mathrm{V}\hat{\mathbf{j}}+\mathbf{H}_\mathrm{V}\hat{\mathbf{k}}$ is the viscous flux vector, and $\hat{\mathbf{n}}$ is the outward unit vector normal to the control volume V.

The vectors in Eq. (3) are defined as follows:

$$\mathbf{U} = \begin{Bmatrix} 1 \\ u \\ v \\ w \end{Bmatrix},$$

$$\mathbf{F}_{\mathrm{I}} = \begin{Bmatrix} u - u_{\mathrm{b}} \\ u(u-u_{\mathrm{b}}) + p \\ v(u-u_{\mathrm{b}}) \\ w(u-u_{\mathrm{b}}) \end{Bmatrix}, \quad \mathbf{G}_{\mathrm{I}} = \begin{Bmatrix} v - v_{\mathrm{b}} \\ u(v-v_{\mathrm{b}}) \\ v(v-v_{\mathrm{b}}) + p \\ w(v-v_{\mathrm{b}}) \end{Bmatrix}, \quad \mathbf{H}_{\mathrm{I}} = \begin{Bmatrix} w - w_{\mathrm{b}} \\ u(w-w_{\mathrm{b}}) \\ v(w-w_{\mathrm{b}}) \\ w(w-w_{\mathrm{b}}) + p \end{Bmatrix},$$

$$\mathbf{F}_{\mathrm{V}} = \frac{1}{Re}\begin{Bmatrix} 0 \\ 2\frac{\partial u}{\partial x} \\ \frac{\partial u}{\partial y} + \frac{\partial v}{\partial x} \\ \frac{\partial u}{\partial z} + \frac{\partial w}{\partial x} \end{Bmatrix}, \quad \mathbf{G}_{\mathrm{V}} = \frac{1}{Re}\begin{Bmatrix} 0 \\ \frac{\partial v}{\partial x} + \frac{\partial u}{\partial y} \\ 2\frac{\partial v}{\partial y} \\ \frac{\partial v}{\partial z} + \frac{\partial w}{\partial y} \end{Bmatrix}, \quad \mathbf{H}_{\mathrm{V}} = \frac{1}{Re}\begin{Bmatrix} 0 \\ \frac{\partial w}{\partial x} + \frac{\partial u}{\partial z} \\ \frac{\partial w}{\partial y} + \frac{\partial v}{\partial z} \\ 2\frac{\partial w}{\partial z} \end{Bmatrix},$$

where the Reynolds number is given by the relation $Re = v/(U_\infty D)$ with v being the kinematic viscosity of the fluid.

2.2. Time-accurate formulation of the artificial compressibility method

The incompressible Navier–Stokes equations are being solved with the method of artificial compressibility (AC). The original form of the artificial compressibility method introduced by Chorin [20] was for steady-state problems with no true time-derivative terms in the formulation. The time-accurate formulation of the artificial compressibility method employed in the present work was first presented by Belov et al. [21] by using the dual time-stepping algorithm of Jameson [22].

In the current time-accurate formulation, a pseudo time-derivative of pressure is added to the continuity equation and pseudo time-derivatives of velocity components are added to the momentum equations. As a result, the momentum equations have true time-derivatives, as well as the pseudo time-derivatives.

The system of conservation laws with the added pseudo-terms can be expressed as:

$$\mathbf{P}\frac{\mathrm{d}}{\mathrm{d}t^*}\int_{V(t)} \mathbf{Q}\,\mathrm{d}V + \mathbf{R}^*(\mathbf{Q}, \mathbf{x}, \dot{\mathbf{x}}) = 0, \tag{4}$$

where the vector $\mathbf{Q}$ contains the primitive variables which are the unknowns of the system of equations, and $\mathbf{P}$ is a diagonal matrix containing the artificial compressibility parameter β acting as a pre-conditioner for the continuity equation:

$$\mathbf{P} = \begin{bmatrix} 1/\beta & 0 & 0 & 0 \\ 0 & 1 & 0 & 0 \\ 0 & 0 & 1 & 0 \\ 0 & 0 & 0 & 1 \end{bmatrix}, \quad \mathbf{Q} = \begin{Bmatrix} p \\ u \\ v \\ w \end{Bmatrix}.$$

The artificial compressibility parameter β controls the speed of artificial pressure waves and also affects the overall convergence rate. Depending on the preconditioning method employed, a more complicated preconditioning matrix which includes the variable β can be used. For the present study, a simple diagonal preconditioning matrix with a constant β in the order of O(100) is used.

Finally $\mathbf{R}^*(\mathbf{Q}, \mathbf{x}, \dot{\mathbf{x}})$ is the semi-discretized (discretized in time and continuous in space) unsteady residual, which consists of the true time-derivative, and the steady-state residual $\mathbf{R}(\mathbf{Q}, \mathbf{x}, \dot{\mathbf{x}})$.

$$\mathbf{R}^*(\mathbf{Q}, \mathbf{x}, \dot{\mathbf{x}}) = \frac{\mathrm{d}}{\mathrm{d}t}\int_{V(t)} \mathbf{U}\,\mathrm{d}V + \mathbf{R}(\mathbf{Q}, \mathbf{x}, \dot{\mathbf{x}}), \tag{5}$$

and the steady-state residual $\mathbf{R}(\mathbf{Q}, \mathbf{x}, \dot{\mathbf{x}})$ of convective and viscous flux terms is defined as follows:

$$\mathbf{R}(\mathbf{Q}, \mathbf{x}, \dot{\mathbf{x}}) = \oint_{S(t)} \left(\mathbf{F}_{\mathrm{I}}\hat{\mathbf{i}} + \mathbf{G}_{\mathrm{I}}\hat{\mathbf{j}} + \mathbf{H}_{\mathrm{I}}\hat{\mathbf{k}} \right) \cdot \hat{\mathbf{n}} \, \mathrm{d}S - \oint_{S(t)} \left(\mathbf{F}_{\mathrm{V}}\hat{\mathbf{i}} + \mathbf{G}_{\mathrm{V}}\hat{\mathbf{j}} + \mathbf{H}_{\mathrm{V}}\hat{\mathbf{k}} \right) \cdot \hat{\mathbf{n}} \, \mathrm{d}S, \tag{6}$$

where $\mathbf{x}$ and $\dot{\mathbf{x}}$ are the time varying position and velocity vectors of the mesh points. The vector $\mathbf{Q}$ contains the primitive variables, which are the pressure and the velocities. Depending on the treatment of the time evolution term in the unsteady residual, the moving mesh source term may or may not arise, and the details of the formulations are presented in the following section.

3. Discretization of the ALE scheme with moving mesh source term

Two different ALE formulations are presented, namely one with the moving mesh source term and the other without such a source term. The difference in the formulation comes from the treatment of the volumetric change in the unsteady term. The spatial discretization scheme using unstructured hybrid meshes is illustrated. Dual time-stepping temporal discretization is presented and the temporal accuracy of the presented ALE scheme is demonstrated via a time-step refinement study. The uniform flow preserving capability of the two ALE formulations is examined.

3.1. ALE formulations with and without the moving mesh source term

The geometric conservation law (GCL) was originally proposed by Thomas and Lombard [23]. The GCL requires that a uniform flow solution is preserved regardless of the mesh motion. The GCL can be directly derived from the continuity equation, Eq. (1), by considering uniform flow everywhere. Then the continuity equation reduces to the geometric conservation law:

$$\frac{\mathrm{d}}{\mathrm{d}t} \int_{V(t)} \mathrm{d}V = \oint_{S(t)} \mathbf{V}_{\mathrm{b}} \cdot \hat{\mathbf{n}} \, \mathrm{d}S. \tag{7}$$

As seen in Eq. (7), the GCL states purely kinematic relations, namely the instantaneous rate of change of a control volume should equal the rate of volume swept by S. This purely geometrical relation can also be interpreted as Leibniz's rule in multi-spatial dimensions. Note that the GCL concerns not only incompressible flows but compressible flows as well, as long as moving meshes are involved.

The system of conservation laws in Eq. (3) can be rewritten as follows:

$$\frac{\mathrm{d}}{\mathrm{d}t} \int_{V(t)} \mathbf{U} \, \mathrm{d}V + \mathbf{R}(\mathbf{Q}, \mathbf{x}, \dot{\mathbf{x}}) = 0. \tag{8}$$

The system of equations as shown in Eq. (8) can be rewritten by using the control volume-averaged conserved variables defined by $\bar{\mathbf{U}} = \frac{1}{V}\int_V \mathbf{U} \, \mathrm{d}V$ as follows:

$$\frac{\mathrm{d}}{\mathrm{d}t}(\bar{\mathbf{U}}V) + \mathbf{R}(\mathbf{Q}, \mathbf{x}, \dot{\mathbf{x}}) = 0. \tag{9}$$

Since the control volume $\mathbf{V}(t)$ and volume-averaged conserved variables $\bar{\mathbf{U}}(t)$ vary smoothly with respect to time, the unsteady term in Eq. (9) can be expanded as:

$$\frac{\mathrm{d}\bar{\mathbf{U}}}{\mathrm{d}t} V + \frac{\mathrm{d}V}{\mathrm{d}t} \bar{\mathbf{U}} + \mathbf{R}(\mathbf{Q}, \mathbf{x}, \dot{\mathbf{x}}) = 0. \tag{10}$$

Finally, the time derivative of the control volume in Eq. (10) can be replaced with a surface integral of the control volume velocity using the GCL as shown in Eq. (7) to obtain:

$$\frac{\mathrm{d}\bar{\mathbf{U}}}{\mathrm{d}t} V + \mathbf{R}(\mathbf{Q}, \mathbf{x}, \dot{\mathbf{x}}) = -\bar{\mathbf{U}} \oint_S \mathbf{V}_{\mathbf{b}} \cdot \hat{\mathbf{n}} \, \mathrm{d}S. \tag{11}$$

We note that since the moving mesh source term is directly derived from the GCL, the system of conservation laws presented in Eq. (11) is inherently equipped with the GCL. Hence the uniform flow is preserved regardless

of the mesh motion, and the GCL is automatically satisfied. An example of temporal discretization (second-order backward difference formula) of the ALE formulation with the moving mesh source term can be expressed as follows:

$$\left(\frac{3\bar{\mathbf{U}}^{n+1}-4\bar{\mathbf{U}}^{n}+\bar{\mathbf{U}}^{n-1}}{2\Delta t}\right)V^{n+1}+\mathbf{R}\left(\mathbf{Q}^{\mathbf{n+1}},\mathbf{x}^{\mathbf{n+1}},\dot{\mathbf{x}}^{\mathbf{n+1}}\right)=\mathbf{S}\left(\bar{\mathbf{U}}^{\mathbf{n+1}},\mathbf{x}^{\mathbf{n+1}},\dot{\mathbf{x}}^{\mathbf{n+1}}\right), \tag{12}$$

where $\mathbf{R}$ is the residual evaluated on the mesh configuration of time t^{n+1} and $\mathbf{S}=-\bar{\mathbf{U}}\oint_S \mathbf{V_b}\cdot\hat{\mathbf{n}}\,\mathrm{d}S$ is the moving mesh source evaluated on the mesh configuration at time t^{n+1}. The moving mesh velocity is approximated with the same time-discretization scheme as for the governing equations as follows:

$$\dot{\mathbf{x}}^{n+1}=\frac{3\mathbf{x}^{n+1}-4\mathbf{x}^{n}+\mathbf{x}^{n-1}}{2\Delta t}.$$

On the other hand, if the unsteady term in Eq. (9) is discretized in time directly without an expansion, the volumetric change of the finite control volume is accounted for by the discretized unsteady term itself and no source term arises. Then, the unsteady term can be discretized by using the following second order backward difference formula:

$$\left(\frac{3\mathbf{U}^{n+1}V^{n+1}-4\mathbf{U}^{n}V^{n}+\mathbf{U}^{n-1}V^{n-1}}{2\Delta t}\right)+\mathbf{R}\left(\mathbf{Q}^{\mathbf{n+1}},\mathbf{x}^{\mathbf{n+1}},\dot{\mathbf{x}}^{\mathbf{n+1}}\right)=0. \tag{13}$$

When this formulation is employed, the residual $\mathbf{R}$, containing the numerical fluxes on the moving meshes, should be evaluated carefully rather than evaluating simply on the mesh configuration at time t^{n+1}. Extensive research has been carried out by Farhat's group about the accurate evaluation of the numerical flux $\mathbf{R}$ so that the time integrator preserves the temporal accuracy and also obeys the GCL [16].

3.2. Spatial discretization with general hybrid meshes

The spatial discretization employed is general to handle hybrid meshes consisting of all four types of computational elements in three dimensions (prisms, hexahedra, tetrahedra and pyramids), as first introduced by Kallinderis and Ahn [24]. A conservative, finite-volume method is presented for solving the incompressible Navier–Stokes equations. A node-centered median dual scheme is used for spatial discretization. An edge-based algorithm is used for the computation of the numerical fluxes. Regarding the viscous flux evaluation at an edge, another conceptual finite volume composed of the union of the cells sharing the edge is used for computing the volume-averaged velocity gradient at the edge midpoint. A dual time-stepping scheme is presented for the time-accurate formulation of the artificial compressibility method.

Typical configurations of node-centered median dual control volumes in two dimensions are shown in Fig. 1. The region indicated by dashed lines around node i represents node-duals. The node-dual around node i is constructed by connecting line segments defined by the edge midpoints and the centroids of the cells sharing node i. The symbols L and R in Fig. 1, denote the left and right sides of the node-dual boundary assuming that the edge is directed outward with respect to node-dual i. In three dimensions, the node dual corresponding to node i is constructed by connecting face segments (instead of lines in two dimensions) defined by edge midpoints, cell centers, and face centers sharing node i.

3.2.1. Convective flux

The convective flux for node-dual i in discrete form can be expressed as:

$$\int_{S_i}(\mathbf{F_I}\mathbf{i}+\mathbf{G_I}\mathbf{j}+\mathbf{H_I}\mathbf{k})\cdot\mathbf{n}\,\mathrm{d}S\approx\sum_{j=1}^{J_i}(\mathscr{F})_j\Delta S_j=\mathbf{C}_i(\mathbf{Q}), \tag{14}$$

where $(\mathscr{F})_j=\mathbf{F_I}n_x+\mathbf{G_I}n_y+\mathbf{H_I}n_z$ is the numerical flux evaluated at the mid-point of the jth neighbor edge, J_i is the number of neighbor edges connected to node i, n_x, n_y, and n_z are the components of the outward unit normal vector of the node-dual boundary associated with edge j, and ΔS_j is the area of the node-dual boundary associated with edge j. The term $\mathbf{C}_i(\mathbf{Q})$ is the net contribution of the convective numerical flux through the control volume boundary (S_i) around node i.

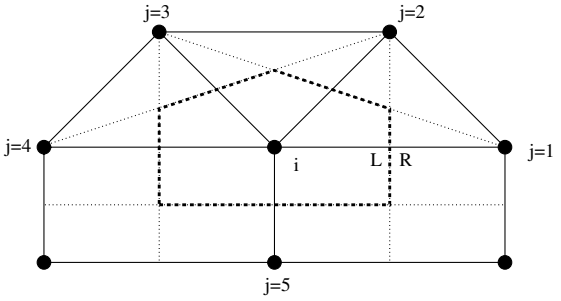

(a) node-dual with mixed type of cells

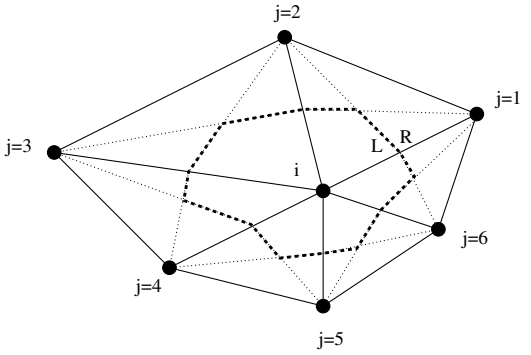

(b) node-dual with triangular cells

Fig. 1. Node-duals around node-i in two dimensions.

By using the central difference scheme, the numerical flux at the edge's midpoint is evaluated via averaging of the fluxes at its two end nodes, as shown in the following equation:

$$(\mathscr{F}_{\text{central}})_j = \frac{1}{2}(\mathscr{F}(\mathbf{Q}_i) + \mathscr{F}(\mathbf{Q}_j)). \tag{15}$$

The surface integral of Eq. (14) is computed in edge-wise fashion. By visiting each edge only once, we compute the flux contribution, and send the flux contribution to the control-volume on one side and an opposite contribution to the other side. This edge-based algorithm does not require any information about cell topology, so the algorithm is suitable for hybrid meshes that include various types of elements in a single computational domain.

Central difference schemes are susceptible to high frequency spurious oscillations triggered by the nonlinear nature of the governing equations. In order to suppress these high frequency oscillations, an additional smoothing term is needed.

For hybrid meshes, oscillations of the solution have been observed by Haselbacher and Blazek [25] when an explicit Runge–Kutta scheme is used in conjunction with the central scheme. The artificial dissipation model proposed by Haselbacher and Blazek can be expressed as follows:

$$\mathbf{D}_i(\mathbf{Q}) = -\sum_{j=1}^{J_i} \sigma_4 \rho_{ij}(\mathbf{Q}_{\mathrm{L}} - \mathbf{Q}_{\mathrm{R}}), \tag{16}$$

where J_i is the number of nodes connected to node i, σ_4 is a coefficient for scaling the artificial dissipation, ρ_{ij} is an estimate of the spectral radius associated with the jth neighbor edge, $\mathbf{Q}_{\mathrm{L}}$ and $\mathbf{Q}_{\mathrm{R}}$ are the linearly reconstructed solutions at the node-dual boundary. A Taylor series expansion is used for this linear reconstruction.

An approximation of the spectral radius scaled by the node-dual boundary associated with the edge j is the following:

$$\rho_{ij} = (|u_n| + c)\Delta S_j, \tag{17}$$

where the velocity normal to the node dual boundary is $u_n = un_x + vn_y + wn_z$, and the artificial speed of sound is defined by $c = \sqrt{u_n^2 + \beta}$ where β is the artificial compressibility parameter.

3.2.2. Viscous flux

In order to evaluate the viscous fluxes through the control volume boundary, the gradients of velocity components have to be pre-computed at each edge. For this computation, another conceptual finite-volume, called edge-dual, is constructed. The edge-dual is composed of the neighbor cells sharing the edge. Various kinds of edge-duals encountered in two-dimensional hybrid meshes are illustrated in Fig. 2.

For the computation of the volume-averaged velocity gradients at each edge, the divergence theorem is used and the surface integration is performed on the edge-dual boundary. For example, computation of the volume-averaged $\frac{\partial u}{\partial x}$ using an edge-dual can be expressed as:

$$\left(\frac{\partial u}{\partial x}\right)_e = \frac{1}{V_e} \oint_{S_e} u n_x \, dS, \tag{18}$$

where V_e is the volume of the edge-dual, and S_e is the boundary of V_e.

Once the velocity gradients are computed at all edges, another edge-wise operation is used for the viscous flux evaluation for node i as shown below.

$$\oint_{S_i} (\mathbf{F}_V \mathbf{i} + \mathbf{G}_V \mathbf{j} + \mathbf{H}_V \mathbf{k}) \cdot \mathbf{n} \, dS \approx \sum_{j=1}^{J_i} (\mathscr{F}_V)_j \Delta S_j = \mathbf{V}_i(\mathbf{Q}), \tag{19}$$

where $(\mathscr{F}_V)_j$ is the viscous flux evaluated at edge j, and is computed as follows:

$$(\mathscr{F}_V)_j = \mathbf{F}_V n_x + \mathbf{G}_V n_y + \mathbf{H}_V n_z.$$

The symbol J_i in Eq. (19) denotes the number of edges connected to node i, ΔS_j is the area of the node-dual boundary associated with the jth edge, and $\mathbf{V}_i(\mathbf{Q})$ is the final contribution of the viscous fluxes to the control-volume around node i.

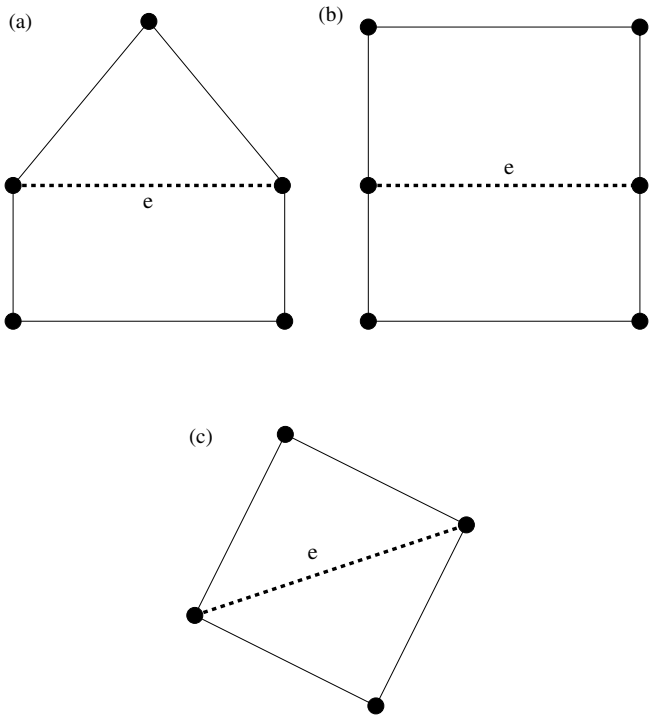

Fig. 2. Edge-duals in two dimensions. Edge-duals are composed of neighbor cells sharing the common edge e.

3.3. Dual time-stepping temporal discretization

The present time-accurate formulation of the artificial compressibility method includes two different time evolution terms; one in true (physical) time t and the other in pseudo-time t^*. First, the true time-derivative term is discretized by using the second order backward difference formula, and then the pseudo time-derivative term is treated until steady state in pseudo-time is reached. Hence, the time-accurate simulation is driven by a series of steady state problems in pseudo-time, as follows:

$$\frac{\mathrm{d}}{\mathrm{d}t^*}(\mathbf{Q}_i V_i) + \mathbf{P}^{-1}\mathbf{R}_i^*(\mathbf{Q}) = 0, \tag{20}$$

where $\mathbf{R}_i^*$ is the unsteady residual for the control volume around node-i, and it includes the discretized true time evolution term, the convective and viscous fluxes, the artificial dissipation term, and the moving mesh source term as defined by:

$$\mathbf{R}_i^*(\mathbf{Q}, \mathbf{x}, \dot{\mathbf{x}}) = \left(\frac{3\mathbf{U}_i - 4\mathbf{U}_i^n + \mathbf{U}_i^{n-1}}{2\Delta t}\right) V_i^{n+1} + \mathbf{R}_i - \mathbf{D}_i - \mathbf{S}_i. \tag{21}$$

In order to advance the solution from the true time t_n to time t_{n+1}, the unsteady residual $\mathbf{R}^*(\mathbf{Q})$ is first constructed by discretizing the true time-derivative with an implicit backward difference formula, and then the steady-state problem shown in Eq. (20) is solved in pseudo-time. Once the steady-state in pseudo-time is reached, the pseudo time-derivative vanishes and the solution advances to the next time step.

The dual time-stepping scheme is driven by the time integration scheme for the pseudo steady-state problem. Therefore, the overall performance of the dual time-stepping scheme is highly dependent on the efficiency of the steady-state solver in pseudo-time:

$$\frac{\mathrm{d}}{\mathrm{d}t^*}\left(\mathbf{Q}_i^k V_i\right) + \mathbf{P}^{-1}\mathbf{R}_i^*(\mathbf{Q}^k) = 0. \tag{22}$$

An iterative method using a 5-stage multistage scheme is used for solving the steady-state problem in pseudo-time. The term k in Eq. (22) is the index of the iteration. This iteration for pseudo time-stepping is referred to as the sub-iteration. In pseudo time-stepping there is no need to preserve the transient temporal accuracy, so local time-stepping is used for convergence acceleration. The 5-stage multistage scheme with point implicit treatment [26] of the diagonal terms is presented below

$$\begin{aligned}
&\mathbf{Q}^{(0)} = \mathbf{Q}^k, \\
&\quad\vdots \\
&\mathbf{Q}^{(l)} = \frac{1}{1+\alpha_l\bar{\lambda}}\left[\mathbf{Q}^{(0)} - \alpha_l \Delta t_i^* \frac{1}{V_i}\mathbf{R}_i^*\left(\mathbf{Q}^{(l-1)}\right) + \alpha_l\bar{\lambda}\mathbf{Q}^{(l-1)}\right], \\
&\quad\vdots \\
&\mathbf{Q}^{k+1} = \mathbf{Q}^{(5)},
\end{aligned} \tag{23}$$

where $\bar{\lambda} = \frac{3}{2}\frac{\Delta t^*}{\Delta t}$, and $\alpha_1, \ldots, \alpha_5$ are optimized coefficients for convergence acceleration to steady state, while Δt_i^* is the local pseudo time step for node i. This multistage scheme is referred to as the hybrid multi-stage scheme to distinguish it from the conventional scheme of evaluating all the fluxes at every stage. A more detailed description of the hybrid multistage scheme for central differences is presented in [27,28].

The point implicit treatment affects only the equations with true time-derivatives, (i.e. the momentum equations). The continuity equation which does not have the true time-derivative is not affected. Hence, for simplicity, the diagonal preconditioning matrix $\mathbf{P}$ is omitted in the point implicit multistage formulation shown in Eq. (23), since its effect on the momentum equations is the same as that of the identity matrix.

3.4. Temporal accuracy of the ALE scheme with the moving mesh source term

Temporal accuracy of the presented ALE scheme is verified by using a time step refinement study. For the geometrically conservative ALE schemes without a moving source term, the temporal accuracy of the backward difference formula has been verified numerically and analytically by means of local truncation error analysis in previous work of Geuzaine et al. [16]. The accuracy of the backward difference scheme applied to the geometrically conservative ALE formulation with the moving mesh source term is investigated here. We present the time step refinement study using a comparison with a reference solution obtained with a time step that is a few orders of magnitude smaller in lieu of the exact solution. A temporal accuracy study by means of local truncation error analysis is also presented by Ahn [29].

In this section, a time step refinement study is presented for the moving mesh simulations of the current ALE scheme with moving mesh source term. The temporal order of accuracy is presented by comparing the solutions with finite time steps to a reference solution obtained using a very small time step. A three-dimensional structured polar mesh ($25 \times 32 \times 11$ nodes) is used, and symmetry boundary condition is used for the flow part along the span-wise direction of the cylinder. The cylinder is modeled as a beam element, and the motion of the cylinder is prescribed.

In order to estimate the order of accuracy of the backward difference formulas of the current ALE scheme, a series of successively refined time-steps ($\Delta t = 0.2, 0.1, 0.05$) are used for the forced excitation problem of the cylinder. Since there is no exact solution for this problem, a reference solution is obtained using a very small time step ($\Delta t = 0.001$) in lieu of the exact solution.

The comparison of the first and second order backward difference formulae in the prediction of hydrodynamic force is presented in Fig. 3. The span averaged lift coefficient (C_L) responses to the harmonically excited cylinder with uniform inflow is presented with a series of successively refined time steps. A clamped-sliding boundary condition is applied, which enforces no-translation/no-rotation at one end of the cylinder ($z = 0$) and free-translation/no-rotation at the other end ($z = L$). The cylinder is deformed by applying excitation to the $z = L$ end as follows:

$$y_{z=L}(t) = \sin(t).$$

For the first order backward difference formula (BDF1), relatively wide deviation of the C_L response from the reference solution is observed. For the second order scheme (BDF2), the C_L histories are more clustered to the reference solution, which indicates better convergence.

The solution with each time step is compared to the reference solution at the non-dimensional time $t = 10.0$. As shown in Eq. (24), the error is measured in the L^2 sense by computing at every nodal point the difference of the solution between the reference and numerical solutions with the various time steps.

$$\mathrm{Error}_{\Delta t} = \sqrt{\frac{\sum_{i=1}^{NI} \|\mathbf{Q}_{\mathrm{ref}} - \mathbf{Q}_{\Delta t}\|_{L^2}^2}{NI}}, \tag{24}$$

where NI is the total number of nodes and $\mathbf{Q}_{\mathrm{ref}}$ is the reference solution obtained with $\Delta t = 0.001$.

Fig. 4 shows the decay of the error as the time step is refined. The first and second order backward difference formulas show first and second order accuracy, respectively. Hence, the time integration schemes used for the current ALE scheme have the same order of accuracy with their fixed mesh counterparts.

The temporal accuracy of the current ALE formulation is confirmed by VIV simulations using time steps of $\Delta t = 0.2$, 0.1, and 0.05. A three-dimensional structured polar mesh ($25 \times 32 \times 11$ nodes) is used around a cylinder, and the cylinder is modeled as a beam element with pinned–pinned end condition, i.e. free-rotation/no-translation at both ends. All flow variables are extrapolated on the boundary normal to the span of the cylinder. The VIV parameters are chosen as $M_{\mathrm{red}} = 2.0$ and $U_{\mathrm{red}}^{\mathrm{beam}} = 2.5$. Detailed description of the structural model for the cylinder and the definition of the VIV parameters (M_{red} and $U_{\mathrm{red}}^{\mathrm{beam}}$) are presented in Section 4. The influence on the VIV of the different time steps is displayed in Fig. 5. For each of the time steps, the vibration periods averaged over the last three cycles are listed in Table 1. The order of convergence for the VIV period, T, is estimated by extrapolation as shown in Eq. (25), and agrees with the formal accuracy of the three point backward difference formula

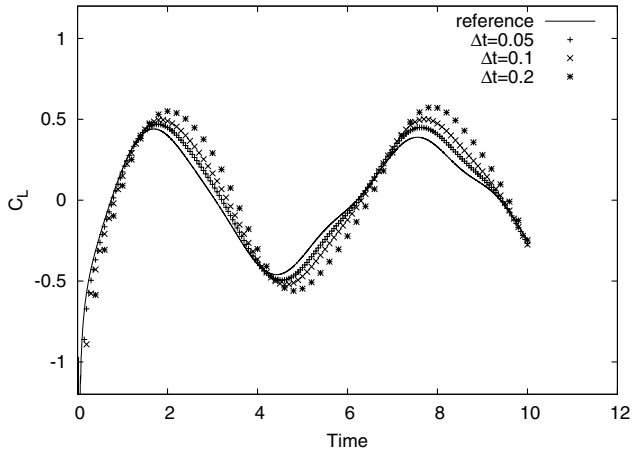

(a) first order backward difference formula (BDF1)

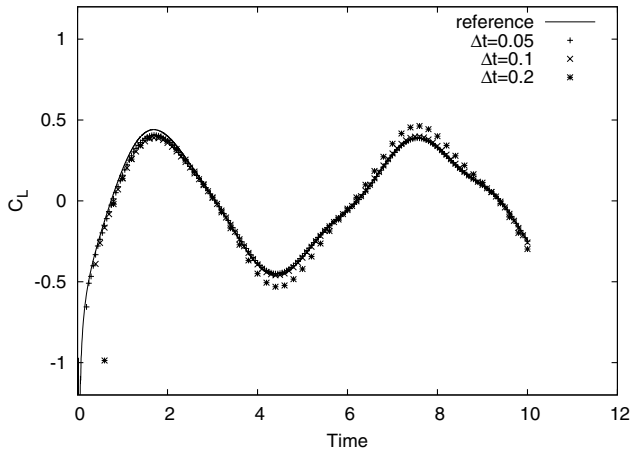

(b) second order backward difference formula (BDF2)

Fig. 3. Span averaged lift coefficient (C_L) responses to the forced excitation of a cylinder. Clamped-sliding end condition is employed and harmonic excitation ($y_{z=L} = \sin(t)$) is applied at the sliding end ($z = L$). $Re = 150$ and $L/D = 5.0$.

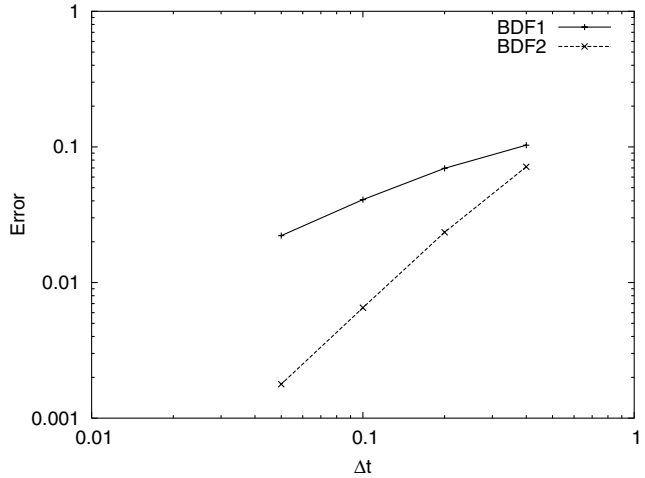

Fig. 4. Temporal accuracy of the backward difference formulas (BDF) for the present ALE scheme. The error is decaying in the order of one for the first order backward difference formula (BDF1) and two for the second order backward difference formula (BDF2).

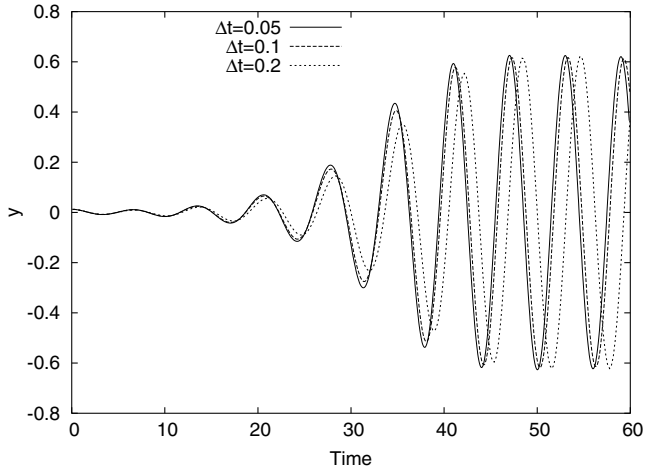

Fig. 5. Time step refinement study using a structured polar mesh ($25 \times 32 \times 11$ nodes). The vertical displacement (y) at the midpoint of the cylinder is displayed with different time steps. The VIV parameter values are: $M_{\text{red}} = 2.0$, $U_{\text{red}}^{\text{beam}} = 2.5$, $L/D = 5.0$ and $Re = 150$.

Table 1
VIV periods averaged over the last three cycles

Δt	VIV period, T
0.2	6.200
0.1	6.025
0.05	6.000

$$\log_2\left(\frac{(T)_{\Delta t=0.2} - (T)_{\Delta t=0.1}}{(T)_{\Delta t=0.1} - (T)_{\Delta t=0.05}}\right) = 2.807. \tag{25}$$

3.5. Effect of the moving mesh source term on preservation of uniform flow

The uniform flow preserving capability of the proposed ALE scheme is demonstrated with the flow simulations over a deforming cylinder. The cylinder is modelled with beam structural elements, and then excited harmonically at one of its ends ($z = L$) in the cross-flow direction (y). In order to demonstrate the uniform flow preserving capability via of the moving mesh source term, three cases are considered. The first case is a fixed cylinder simulation, the second case is a deforming cylinder simulation using the ALE formulation with the moving mesh source as presented in Eq. (12), and the third case is that of a deforming cylinder using the ALE formulation without the source term as shown in Eq. (13).

The cylinder modelled with a beam element is excited harmonically by the following relation:

$$y(t)_{z=L} = \sin(t).$$

The cylinder motion causes the mesh to deform accordingly via use of a movement weight function, $w(r)$, defined as:

$$w(r) = \max\left(\frac{r_{\text{deform}} - r}{r_{\text{deform}} - r_o}, 0\right),$$

where r is the distance from the origin on the plane normal to the cylinder span direction, r_o is the radius of the cylinder, and r_{deform} is the radius of the sub-domain of the deforming mesh which can be chosen as the shortest distance to the far field boundary. The weight function is one on the cylinder and decreases linearly to zero as we move away from the wall. By using the deformation weight function the mesh points on the cylinder follow its curvature exactly. Fig. 6 shows the moving mesh around the structure under deformation.

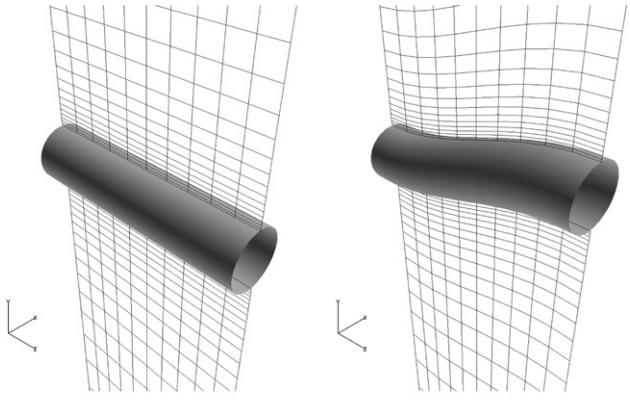

(a) undeformed ($y_{z=L} = 0.0$) (b) deformed ($y_{z=L} = 1.0$)

Fig. 6. Forced excitation of the cylinder in the cross-flow direction. A three-dimensional structured mesh is used ($L/D = 4.0$). A prescribed motion of $y_{z=L} = \sin(t)$ is applied with clamped-sliding end conditions.

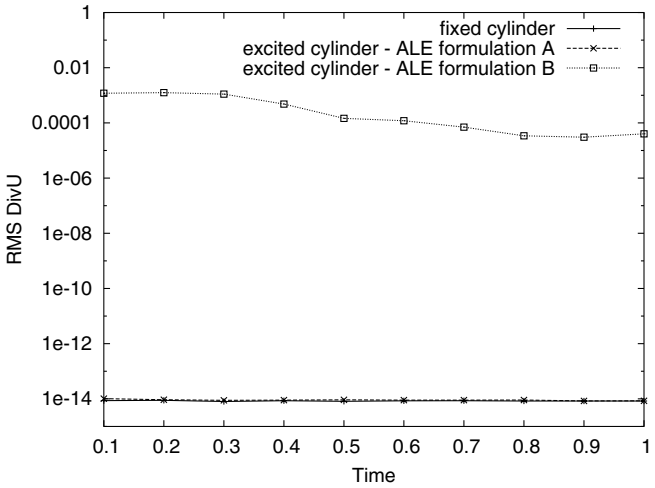

Fig. 7. Comparison of ALE formulations in terms of the uniform flow preserving capability. The ALE formulation A corresponds to the formulation with the moving mesh source term as shown in Eq. (12), and formulation B refers to the ALE scheme with no such source term as presented in Eq. (13). Uniform flow condition is applied for flow everywhere on the boundary.

In Fig. 7, we present a comparison of the divergence of the velocity field for the three cases; fixed cylinder, deforming cylinder with the ALE formulation using the moving mesh source (formulation A) and deforming cylinder with the ALE formulation without use of the source term (formulation B). It is clear that, with the ALE formulation of moving mesh source term, the divergence of the velocity field remains machine-zero and the uniform flow is preserved regardless of the mesh motion. With the ALE formulation with no such source term, the divergence of the velocity field stays around the order of $O(10^{-4})$, which indicates that the uniform flow is not preserved. Hence, it can be concluded that the proposed ALE formulation with the moving mesh source term is geometrically conservative regardless of mesh motion.

4. Equation of motion for the cylinder

The structure is modelled as a rigid body in two dimensions and as flexible cylinder in three dimensions. For both cases, the structure moves freely in the cross-flow direction (y) only, which is the dominant motion of vortex-induced vibrations. The non-dimensional version of the equations of motion for the structure is introduced, both in two and three dimensions.

4.1. The equation of motion for the cylinder in two dimensions

Our structural model for the two-dimensional cylinder is the same one presented by Schulz and Kallinderis [17], and its non-dimensional version can be expressed as follows:

$$\ddot{y} + \left(\frac{4\pi\zeta}{U_{\text{red}}}\right)\dot{y} + \left(\frac{4\pi^2}{U_{\text{red}}^2}\right)y = \left(\frac{1}{2M_{\text{red}}}\right)C_{\text{L}}(t), \tag{26}$$

where $U_{\text{red}} = \frac{U_\infty}{f_n D}$ is the reduced velocity, f_n is the natural frequency of the structure, $M_{\text{red}} = \frac{m}{\rho_\infty D^2}$ is the reduced mass, while y is the displacement of cylinder in the cross-flow direction, and ζ is the non-dimensional damping coefficient. The symbol m denotes the mass of the cylinder, and ρ_∞ is the density of the fluid. The structural damping is neglected in the present work.

The reduced mass M_{red} scales the hydrodynamic forces on the right-hand side, and U_{red} scales the stiffness of the structure. As U_{red} is increased, the period of the structural vibration becomes longer and the equation represents a more flexible structure.

4.2. The equation of motion for the cylinder in three dimensions

The cylinder shown in Fig. 8 is modelled with structural beam elements of four degrees of freedom $(v_1, \theta_1, v_2, \theta_2)$. The direction of the cross-flow displacement (v) coincides with the y-axis, and the direction of the rotational degree of freedom (θ) is in the negative x-direction to be consistent with the sign convention of the beam element as indicated in the figure.

Applying Lagrange's equation with respect to each of the four degrees of freedom yields the set of equations of motion, as follows:

$$\mathbf{M}\ddot{\mathbf{q}}(t) + \mathbf{K}\mathbf{q}(t) = \mathbf{f}(t), \tag{27}$$

where $\mathbf{M}$ and $\mathbf{K}$ are the mass and stiffness matrices, $\mathbf{q}$ is the vector containing the degrees of freedom, and $\mathbf{f}$ is the vector of external forces corresponding to each degree of freedom. The mass and stiffness matrices can be obtained from structural dynamics references, for example [30].

The normalized velocities, length, and time are as follows:

$$v^* = \frac{v}{D}, \quad L^* = \frac{L}{D}, \quad t^* = \frac{t}{D/U_\infty}.$$

The system of equations becomes:

$$\mathbf{M}^*\ddot{\mathbf{q}}^*(t^*) + \frac{1}{L^4}\frac{EI}{\rho_s A}\left(\frac{D}{U_\infty}\right)^2 \mathbf{K}^*\mathbf{q}^*(t^*) = \frac{\rho D^2}{\rho_s A}\frac{D}{L}\mathbf{f}^*(t^*), \tag{28}$$

where the non-dimensional mass and stiffness matrices have the same form as their dimensional counterparts in Eq. (27).

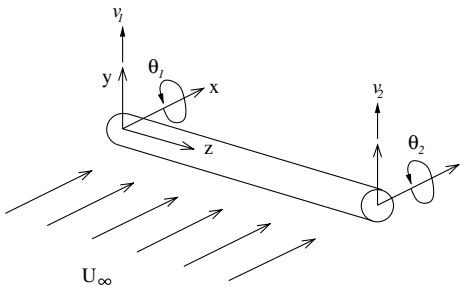

Fig. 8. The structural model in three dimensions.

The system of equations of motion in non-dimensional form can be further simplified by introducing the two non-dimensional parameters of $U_{\text{red}}^{\text{beam}}$ and M_{red}:

$$\mathbf{M}^*\ddot{\mathbf{q}}^*(t^*) + \left(\frac{4\pi^2}{U_{\text{red}}^2}\right)\left(\frac{1}{L^{*4}}\right)\mathbf{K}^*\mathbf{q}^*(t^*) = \left(\frac{1}{M_{\text{red}}}\right)\left(\frac{1}{L^*}\right)\mathbf{f}^*(t^*), \tag{29}$$

where the reduced velocity, $U_{\text{red}}^{\text{beam}}$, is defined as:

$$U_{\text{red}}^{\text{beam}} = \frac{U_\infty}{f_n D}, \tag{30}$$

with the effective natural frequency of the structure, ω_n, shown below.

$$\omega_n = \frac{1}{D^2}\sqrt{\frac{EI}{\rho_s A}} = 2\pi f_n.$$

Notice that unlike the structural model in two-dimension, the stiffness of the structure depends not only on the $U_{\text{red}}^{\text{beam}}$, but also on the non-dimensional length of the cylinder $L^* = L/D$. This is because our definition of reduced velocity is based on a unit-length beam. For a given length (L/D) of the cylinder, the reduced velocity affects the bending stiffness of the structure, and the stiffness of the structure also affects the natural frequency of the bending vibration.

The main objective of this simulation is in the vortex-induced vibration of the cylinder at its resonant state, namely *lock-in* state. Hence the value of U_{red} is chosen so that its natural frequency of bending vibration of interest, typically its first or second mode, is approximately equal to the natural frequency of vortex shedding over a fixed cylinder.

The reduced mass, M_{red}, which is a ratio of the mass of the structure to the mass of the fluid displaced by the structure, is defined in the same way as in two-dimensions:

$$M_{\text{red}} = \frac{\rho_s A}{\rho D^2}. \tag{31}$$

This reduced mass represents the inertia of the structural system with respect to the surrounding fluid. Hence, a smaller mass ratio implies a bigger influence from the flow. The mass ratio of the marine cables in water varies between 1 and 10, and we used the representative mass ratio of $M_{\text{red}} = 2.0$ [31,32] throughout the simulations.

5. Fluid and structure coupling methods

Two different coupling methods are presented, namely weak and strong. Improved stability and convergence of the strong coupling is emphasized. The strong coupling is based on a predictor–corrector method, and it is presented for three-dimensional flexible cylinder applications.

5.1. Comparison of weak and strong couplings

If the flow and structural solvers are being solved separately, then their interaction can be implemented either in a strong coupling method or in a weak coupling method depending on how the information between the two solvers is communicated.

In the weak coupling strategy as shown in Fig. 9, the solution of the flow field at the next time step is computed using the structural configuration at the previous time step. Once the solution of the flow field is obtained at each time level, the new forces acting on the structure are sent to the structural solver in order to compute the new position of the structure at the next time step. This simple loop advances the flow and structural solutions by one time step. The flow-induced forces on the structure come from the solution on the mesh configuration of the previous time level, hence this method is also referred to as a *staggered* or *loosely* coupled scheme. The weak coupling method is popular because it does not require major modification of pre-existing flow and structural solvers. Use of small time steps is a consequence of this coupling method. The loose coupling of fluid and structure interactions can be found among others in [17,33].

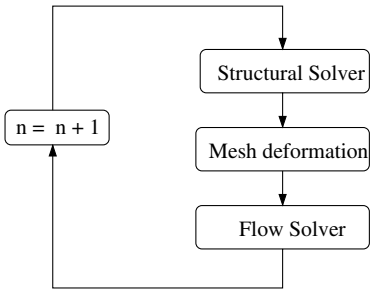

Fig. 9. Weak coupling: the solution of the flow field is obtained at each time level, and then the new forces acting on the structure are sent to the structural solver in order to compute the new position of the structure at the next time step.

The larger time steps that can be used for the flow solution with an implicit scheme may have to be reduced for marching the structure solution, thus necessitating an implicit scheme for the structure, as well. The present strong coupling employs iterations between the two solution procedures at each time step, and this makes their coupling stable even with relatively large time steps.

The present implicit formulation of the flow solution method driven by the dual time-stepping can be easily applied to strongly coupled simulation of fluid–structure interactions. Alonso and Jameson [34] introduced a strong coupling by updating the structural configuration after several iterations of the flow solution. In their scheme, both the flow and structure solution methods use dual time-stepping. More recently, Chen et al. [19] applied a dual time-stepping scheme to achieve strong coupling by updating the structure solution after each iteration of their line Gauss–Seidel method used for the flow solution.

A new strong coupling method is proposed and compared to the traditional weak coupling approach. It is based on a predictor–corrector (PC) method. The PC method is well suited for the present dual time-stepping scheme of the flow solver, and improves the stability of the coupled simulation with the least modification of pre-existing solvers, and with minimum extra memory storage. In fact, the strong coupling via the PC method can be thought of as a unified formulation of the weak and strong couplings. If there is no corrector step employed, then the coupling is in the weak manner. Any explicit scheme can be used for the predictor step, and any implicit scheme can be used for the corrector. The correction iteration can be performed until some criterion of convergence is met. In the present work, the number of corrector iterations is fixed in advance, provided that the stable coupling of fluid and structure interaction is assured, as delineated in Fig. 10. The number of corrector iterations (μ) can be small such as two or three, provided that the predictor step employs sufficiently small time steps. For large time steps, the number of corrector iterations can be as large as the number of dual time steps for the flow part. In this case, the corrector step can be invoked at each sub-iteration of the dual time-stepping loop.

For strong coupling with multiple corrector steps, it is not necessary to converge the flow solution fully at each corrector iteration provided that the flow solution if fully converged at the last corrector step. In the most computationally demanding case, the corrector step can be invoked after each sub-iteration of the flow solver. In this case, the flow–structure coupling loop becomes essentially the same as the pseudo-time-stepping loop of the flow solver.

The predictor step is followed by a new evaluation of the flow field and each corrector step is also followed by a new evaluation of the flow field. This procedure can be represented as

$$PE \underbrace{CE \cdots CE}_{\text{corrector iteration}},$$

where P denotes the predictor step, C represents the corrector step, and E refers to the evaluation of the flow field. When the number of corrector iterations is fixed to be μ, the predictor–corrector method can be expressed more conveniently as $PE(CE)^{\mu}$. The update of the flow field following the last corrector step may be omitted, but completing the PC loop with a flow solution evaluation gives better stability. Hence, we always solve the flow field whenever a new structural configuration is obtained. For the PC method with μ corrector iterations, the total number of evaluations of the flow field is $\mu + 1$. The strong coupling using the PC method reduces to the weak coupling when the corrector iteration loop is omitted. The corrector step is invoked after

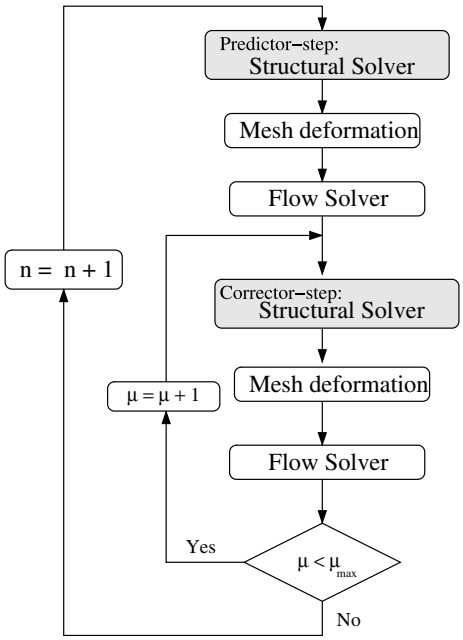

Fig. 10. Strong coupling using predictor–corrector scheme with a fixed number of corrector steps.

several sub-iterations of the flow part, but if the time step is large or if the solution changes rapidly in time, the corrector step can be invokes at each sub-iteration.

A comparison of the two coupling methods is presented in Fig. 11 for vortex-induced vibration in two dimensions. VIV parameters are chosen as $U_{red} = 4.0$ and $M_{red} = 2.0$, and the time step selected as $\Delta t = 0.4$ and $Re = 150$. For the strong coupling, the flow and structure interaction is stable, but the weak coupling process starts with oscillations and eventually diverges. The cylinder was displaced ($y_0 = 0.1$) initially in order to initiate VIV immediately. The same number of sub-iterations was used for the flow part for both the weak and strong couplings per each true time step. The structural solver was called only once in the weak coupling solution process. In the strong coupling it was called each time after a sub-iteration of the flow solver. Each sub-iteration of the flow solver is followed by a structural solver step, hence the pseudo-iteration of the dual time-stepping is essentially the same as the coupling iteration.

Even with invoking the structural solver after each sub-iteration of the flow solver (the most computationally demanding way in strong coupling), the computational cost of the strong coupling is just ~32% higher than the cost of the weak coupling. The weak coupling solution process takes about 15 min, and the strong coupling takes about 19.5 min on a Pentium 4 1.7 GHz laptop for the unsteady simulation up to $Time = 10.0$. This is because most of the CPU time is spent by the flow part.

5.2. Solution of the structures problem via a predictor–corrector method

We present the PC method to solve the equation of motion for the structure. We focus the presentation here on the three-dimensional structural model described with beam elements.

In the present study, the central difference scheme in time is used for the predictor, and the trapezoidal scheme is used for the corrector. Both schemes are second order accurate in time, hence this pair (central-trapezoidal) of the PC method is expected to be second order accurate. Since the time integration scheme of the flow solver is also second order (second order backward difference formula), the current choice of the PC pair should not deteriorate the temporal accuracy when it is coupled with the flow solver.

Once the global mass and stiffness matrices are assembled and proper boundary conditions are applied, the governing equations of the bending vibration can be rewritten as a set of coupled second order ordinary differential equations with a given set of initial conditions as follows.

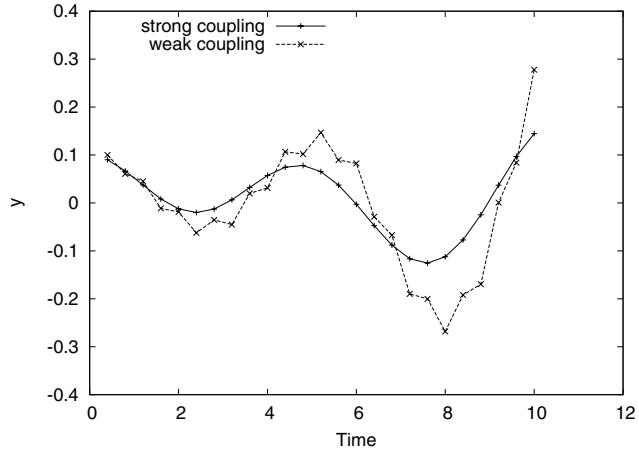

(a) crossflow displacement of the cylinder

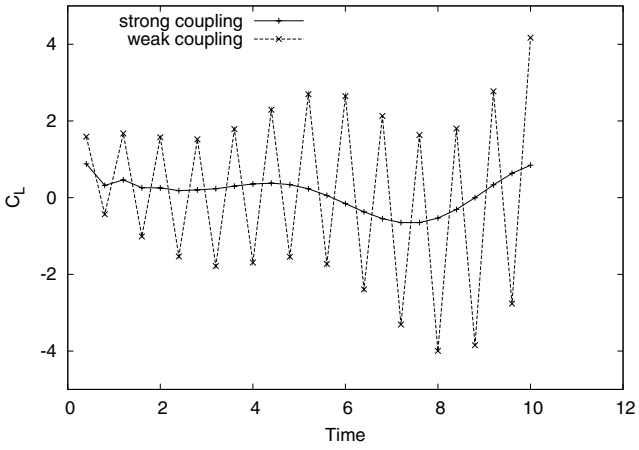

(b) lift coefficient (C_L) on the cylinder

Fig. 11. Comparison of strong and weak couplings. The values of the relevant parameters are: $U_{\text{red}} = 4.0$, $M_{\text{red}} = 2.0$, $\Delta t = 0.4$, and $Re = 150$.

$$\mathbf{M}\ddot{\mathbf{y}}(t) + \mathbf{K}\mathbf{y}(t) = \mathbf{f}(t), \quad \mathbf{y}(0) = \mathbf{y}_0, \quad \dot{\mathbf{y}}(0) = \dot{\mathbf{y}}_0, \tag{32}$$

where $\mathbf{M}$ and $\mathbf{K}$ are the global mass and stiffness matrices, $\mathbf{y}$ are the unknown degrees of freedom and $\ddot{\mathbf{y}}$ are the corresponding accelerations, while $\mathbf{f}$ is the external load vector due to the flow around the cylinder. Further, $\mathbf{y}_0$ and $\dot{\mathbf{y}}_0$ are the initial conditions. The equation of motion in Eq. (32) is in non-dimensional form, and all the $*$'s representing the non-dimensional quantities are omitted for simplicity.

Any explicit/implicit pair can be used for the predictor/corrector method. For the predictor of the present work, the central difference scheme with lagged approximation of the first derivative is used because of its popularity in structural dynamics. For the corrector step, the unconditionally stable trapezoidal scheme is used. This trapezoidal method can be considered as a special case of the Newmark method with average acceleration [35].

The central difference scheme used for the predictor can be derived by using the following central differenced acceleration:

$$\ddot{\mathbf{y}}_n = \frac{1}{\Delta t^2}(\mathbf{y}_{n+1} - 2\mathbf{y}_n + \mathbf{y}_{n-1}), \tag{33}$$

and a velocity which is lagging half a time step as follows:

$$\dot{\mathbf{y}}_n \approx \dot{\mathbf{y}}_{n-\frac{1}{2}} = \frac{1}{\Delta t}(\mathbf{y}_n - \mathbf{y}_{n-1}). \tag{34}$$

Even with the lagged approximation of the velocity, the central difference scheme is reported to be second order accurate for the system of small damping [35]. Hence, the central difference scheme for the current structural model with no damping can be expected to be second order accurate.

By using the central differenced acceleration of Eq. (33), the velocity of Eq. (34), and the equation of motion (29), the predictor scheme can be expressed as follows:

Predictor

$$\mathbf{y}_{n+1}^{(\mu=0)} = \Delta t^2 \mathbf{M}^{-1}(\mathbf{f}_n - \mathbf{K}\mathbf{y}_n) + \mathbf{y}_n + \Delta t \dot{\mathbf{y}}_{n-\frac{1}{2}},$$
$$\dot{\mathbf{y}}_{n+1}^{(\mu=0)} \approx \dot{\mathbf{y}}_{n+\frac{1}{2}}^{(\mu=0)} = \frac{1}{\Delta t}\left(\mathbf{y}_{n+1}^{(\mu=0)} - \mathbf{y}_n\right).$$

By using the trapezoidal rule, the displacement and velocity can be expressed as:

$$\mathbf{y}_{n+1} = \mathbf{y}_n + \frac{\Delta t}{2}(\dot{\mathbf{y}}_n + \dot{\mathbf{y}}_{n+1}),$$
$$\dot{\mathbf{y}}_{n+1} = \dot{\mathbf{y}}_n + \frac{\Delta t}{2}(\ddot{\mathbf{y}}_n + \ddot{\mathbf{y}}_{n+1}).$$

The velocity and acceleration for the next time step can be derived from the above relation

$$\dot{\mathbf{y}}_{n+1} = \frac{2}{\Delta t}(\mathbf{y}_{n+1} - \mathbf{y}_n) - \dot{\mathbf{y}}_n,$$
$$\ddot{\mathbf{y}}_{n+1} = \frac{4}{\Delta t^2}(\mathbf{y}_{n+1} - \mathbf{y}_n) - \frac{4}{\Delta t}\dot{\mathbf{y}}_n - \ddot{\mathbf{y}}_n.$$

Using the equation of motion (Eq. (29)) and the above relations, the corrector scheme can be expressed as:

Corrector

for $i = 1, \ldots, \mu_{\max}$

$$\mathbf{y}_{n+1}^{(\mu)} = \left(\frac{4}{\Delta t^2}\mathbf{M} + \mathbf{K}\right)^{-1}\left(\mathbf{f}_{n+1}^{(\mu-1)} + \mathbf{M}\left(\frac{4}{\Delta t^2}\mathbf{y}_n + \frac{4}{\Delta t}\dot{\mathbf{y}}_n + \ddot{\mathbf{y}}_n\right)\right)$$
$$\dot{\mathbf{y}}_{n+1}^{(\mu)} = \frac{2}{\Delta t}\left(\mathbf{y}_{n+1}^{(\mu)} - \mathbf{y}_n\right) - \dot{\mathbf{y}}_n$$

end

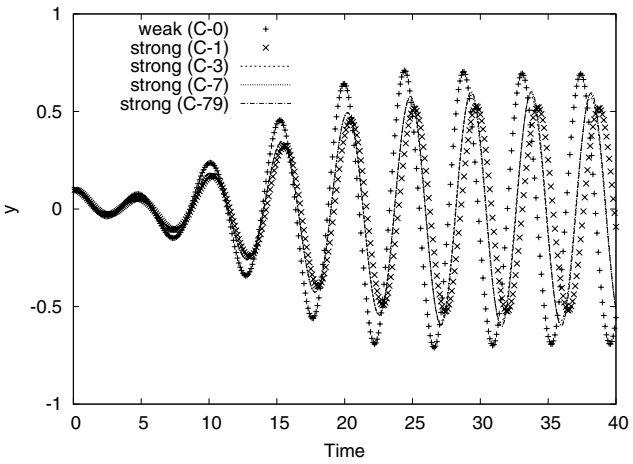

Fig. 12. Convergence of strong coupling with number of corrector iterations for the case of a two-dimensional hybrid mesh simulation. The solution parameters are: $M_{\text{red}} = 2.0$, $U_{\text{red}} = 4.0$, $\Delta t = 0.1$, and $Re = 150$. The weak coupling corresponds to zero corrector iterations (C-0), and the family of strong couplings is presented with different corrector iterations (C-1, C-3, C-7, and C-79).

The corrector iteration is performed until it meets the maximum number of iterations ($\mu_{\max}$).

The influence of the number of corrector iterations on the solution is examined in Fig. 12 which shows the displacement history of the cylinder in two dimensions using a hybrid (quadrilateral/triangles) mesh. The simulation parameters are: $M_{\text{red}} = 2.0$, $U_{\text{red}} = 4.0$, $Re = 150$, which are the same conditions as in Fig. 11, but with smaller time steps ($\Delta t = 0.1$). The case (C-0) corresponds to no corrector iterations, which is the weak coupling, and different numbers of corrector steps are employed (C-1, C-3, C-7, and C-79). The VIV displacement of the structure is converging with increasing number of corrector iterations and only three correction steps (C-3) gives an almost converged result for the present case.

5.3. Temporal accuracy of weak and strong couplings

A time step refinement study is performed to check the temporal accuracy of the proposed coupling methods. The initial time step is chosen so that the coupling is stable for both the weak and strong cases, and it is refined twice. The same two-dimensional hybrid mesh is used as for the case of Fig. 12. For the weak coupling, the structural part is solved only once per time step with the central difference scheme. For the strong coupling,

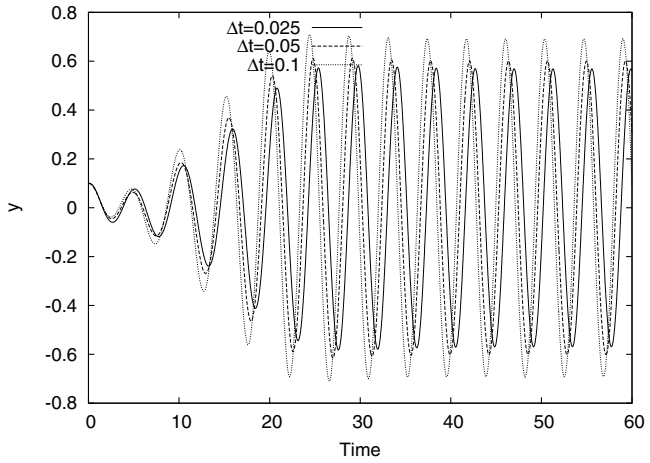

(a) weak coupling

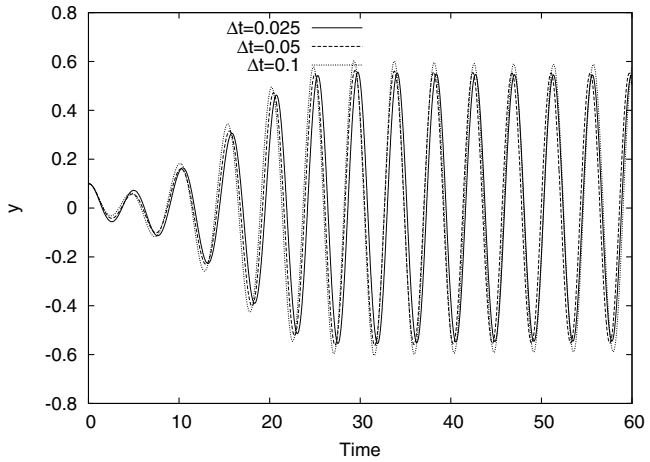

(b) strong coupling

Fig. 13. Time step refinement study of the weak and strong couplings for the case of VIV simulations. The case parameters are: $M_{\text{red}} = 2.0$, $U_{\text{red}} = 4.0$, and $Re = 150$.

Table 2
Time step refinement study via the convergence of the period (T) and the maximum amplitude (y_{max}) of VIV

Δt	Weak coupling		Strong coupling	
	T	y_{max}	T	y_{max}
0.1	4.330	0.691	4.390	0.587
0.05	4.300	0.600	4.315	0.551
0.025	4.297	0.568	4.303	0.544

The periods and maximum amplitudes are calculated by averaging the last 10 cycles of the unsteady simulations.

the structural problem is solved after each evaluation of the flow part using the trapezoidal scheme. The result is displayed in Fig. 13. The periods (T) and maximum amplitudes (y_{max}) of the two coupling methods are given in Table 2. The periods and maximum amplitudes are calculated by averaging the last 10 cycles of the unsteady simulations.

For the weak coupling, the amplitude of the VIV is clearly overpredicted for the same time step size compared to the strong coupling scheme result. A small phase shift is observed for large time steps of the weak coupling, and we believe this is due to the period contraction error of the central difference scheme [35]. Since both the weak and strong couplings use second order accurate schemes for the structural part, it can be expected that both couplings are second order accurate in time. This is confirmed using the VIV periods from the present time step refinement study as follows:

$$\log_2\left(\frac{(T)_{\Delta t=0.1}-(T)_{\Delta t=0.05}}{(T)_{\Delta t=0.05}-(T)_{\Delta t=0.025}}\right)_{\text{weak}} = 3.321,$$
$$\log_2\left(\frac{(T)_{\Delta t=0.1}-(T)_{\Delta t=0.05}}{(T)_{\Delta t=0.05}-(T)_{\Delta t=0.025}}\right)_{\text{strong}} = 2.643.$$

The slope of the convergence curve is higher than two. However, for the maximum amplitudes of the VIV, the weak coupling shows slower time-convergence with a slope of about 1.5, while the strong coupling slope is higher than two as shown below:

$$\log_2\left(\frac{(y_{max})_{\Delta t=0.1}-(y_{max})_{\Delta t=0.05}}{(y_{max})_{\Delta t=0.05}-(y_{max})_{\Delta t=0.025}}\right)_{\text{weak}} = 1.507,$$
$$\log_2\left(\frac{(y_{max})_{\Delta t=0.1}-(y_{max})_{\Delta t=0.05}}{(y_{max})_{\Delta t=0.05}-(y_{max})_{\Delta t=0.025}}\right)_{\text{strong}} = 2.362.$$

6. Applications of the ALE scheme to the strongly coupled simulation of vortex-induced vibrations (VIV)

The strong coupling method and ALE formulations presented in the previous sections are applied to the simulations of vortex-induced vibration of a cylinder in two and three dimensions.

6.1. Two-dimensional simulations of vortex-induced vibration

The present ALE scheme is applied to the simulation of VIV in two dimensions. It has been reported [31,36] that the maximum amplitude of the cylinder oscillations is bounded by ~1.0 diameter, independently of the flow condition or structural configuration. By using a single degree-of-freedom model of the structure, the VIV of a cylinder is simulated. The current simulations are compared with other computational and experimental results in Table 3.

In the table, all of the computational results are from two-dimensional simulations. The present simulation shows good agreement in terms of the maximum vibration amplitude ($y = 0.5$–0.6) with the other computational results. However, the maximum amplitude of the VIV is below the experimental result, whose maximum amplitude of the vibration is $y \sim 1.0d$. Newman and Karniadakis [31] pointed that this discrepancy may be due to absence of the three-dimensionality effect and turbulence from high Reynolds number flows. Even

Table 3
Comparison of the present two-dimensional VIV simulations with other computational and experimental results

	Re	M_{red}	U_{red}	Max y
Current simulation	150	2.0	5.0	0.54
Current simulation	100	2.0	5.0	0.53
Schulz and Kallinderis	110	–	6.13	0.43
Newman and Karniadakis	100	1.0–10.0	–	0.5–0.6
Griffin	300–10^6	–	–	~1.0

The results of Schulz and Kallinderis [17] and Newman and Karniadakis [31] are from two-dimensional simulations, and Griffin's [36] result is from experiments.

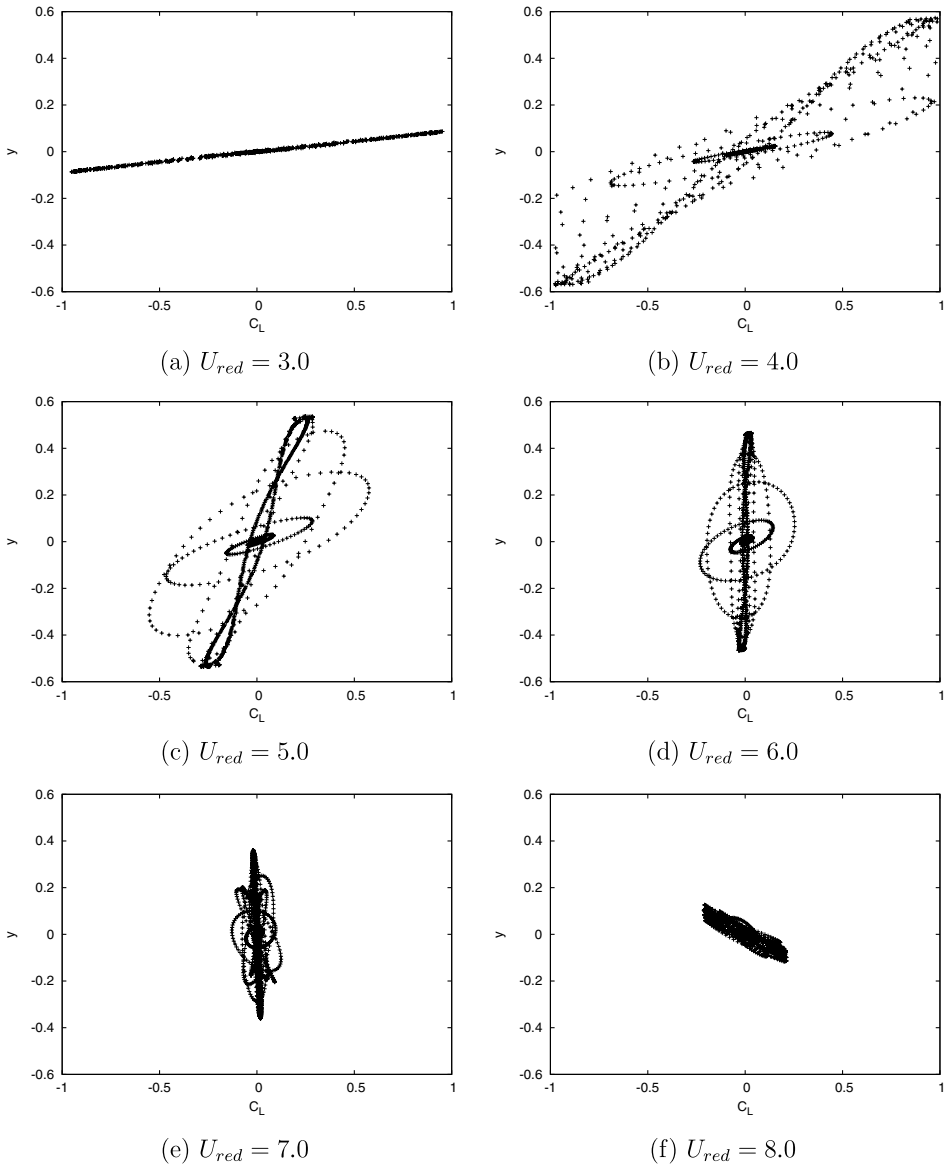

Fig. 14. Two-dimensional VIV ($Re = 150$, $M_{red} = 2.0$). Phase changes between the lift coefficient (C_L) and cross-flow vibration amplitude (y) with different values of the structural stiffness attained by varying U_{red}. The smaller U_{red}, the stiffer the structure is for a given M_{red}. For $U_{red} = 4.0$ as shown in (b) and (c), y reaches it's maximum amplitude (~0.6) and C_L and y is in-phase. As U_{red} increases further, the amplitude of y diminishes and C_L and y become out-of-phase.

though the two-dimensional simulations underpredict the amplitudes of VIV, the boundedness of VIV amplitude in resonance (lock-in regime) is a promising result for the further extension towards three-dimensional high Reynolds flow simulations.

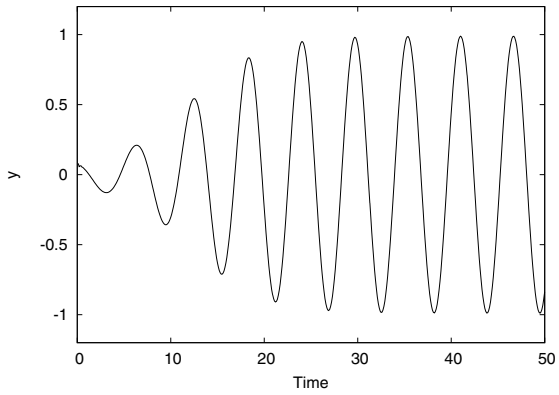

(a) crossflow displacement at sliding end ($y_{z=L}$)

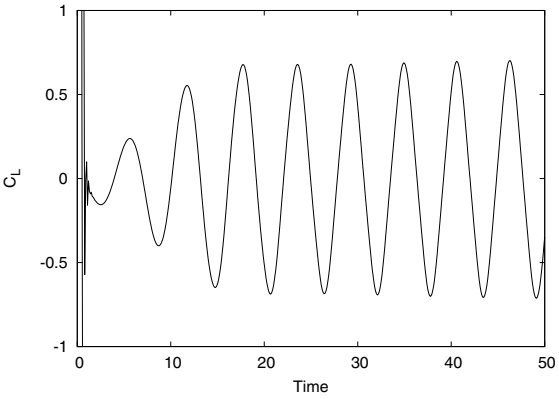

(c) span averaged lift coefficient (C_L)

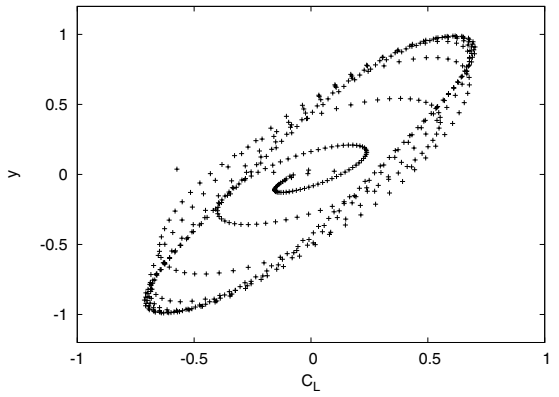

(c) phase portrait

Fig. 15. Vortex-induced vibration of a cylinder in three dimensions using a general hybrid mesh. The VIV is in the lock-in regime ($y_{\max} \sim 1.0$), and C_{L} and y are in-phase as shown in (c). The clamped-sliding end condition is applied for the cylinder, and a symmetry boundary condition is applied for the flow for the span wise direction of the cylinder. The main simulation parameters are: $Re = 150$, $M_{\mathrm{red}} = 2.0$, $U_{\mathrm{red}}^{\mathrm{beam}} = 1.2$ and $L/D = 5.0$.

6.2. Phase transition of C_L and y within the resonance (lock-in) regime

For a given structure, its stiffness can vary by changing U_{red}. The higher U_{red} represents the more flexible structure and vice versa. We vary the stiffness of the cylinder by changing U_{red} within the interval of values (lock-in regime), which typically yield vortex-induced vibrations, and see if there is a certain mode in phase between the hydrodynamic force (C_L) and the cross-flow VIV amplitude (y). The results are presented in Fig. 14. For $U_{red} = 3.0$, which is the case of the stiffest structure, the VIV amplitude is very small and below the maximum amplitude of the lock-in regime. For $U_{red} = 4.0$–5.0, the VIV reaches its maximum amplitude ($y \sim 0.6$), and C_L and y are in-phase. As U_{red} is increased to 6.0–7.0, there appears to be small dependency between C_L and y. Finally, for $U_{red} = 8.0$ (the most flexible structure), C_L and y are out-of-phase and the amplitude of VIV diminishes.

6.3. Three-dimensional simulation of VIV with deformable general hybrid meshes

Vortex-induced vibration of a cylinder in three dimensions is simulated with a deforming general hybrid mesh. The present general hybrid mesh (GHM) contains all four types of elements in a single computational domain (hexahedra, prisms, tetrahedral, and pyramids). The GHM is employed for showing its effectiveness not only for the fixed mesh simulation but also for moving mesh problems, such as fluid–structure interactions or aeroelasticity problems. The clamped-sliding boundary condition is applied for the beam, and the symmetry boundary condition is applied for the flow along the span wise direction.

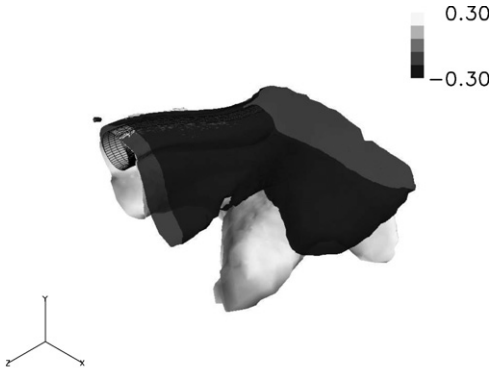

(a) isosurfaces of spanwise vorticity at upstoke

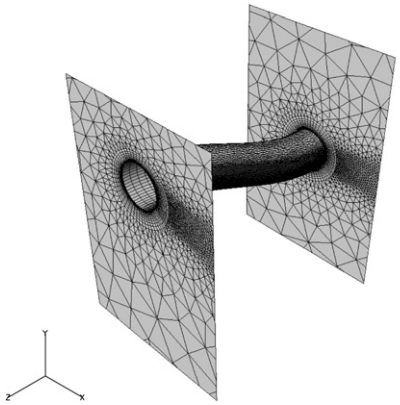

(b) deformed mesh configuration at upstoke

Fig. 16. Three-dimensional VIV simulation with a deforming general hybrid mesh ($Re = 150$, $M_{red} = 2.0$, $U_{red}^{beam} = 1.2$ and $L/D = 5.0$).

The VIV result is presented in Fig. 15. In order to initiate the VIV immediately and save computational time, the initial configuration of the cylinder is disturbed initially at the right end ($z = L$). The oscillation of the initial response of C_L is due to this disturbance and impulsively starting of the flow simulation. The VIV is in the lock-in regime, and the hydrodynamics force (C_L) and cross-flow amplitude are in-phase. The maximum amplitude of the vibration is $y_{max} \sim 1.0$, and this is in better agreement with the experimental result [36] than in the two-dimensional simulation. This increased maximum amplitude of the cross-flow vibration ($y_{max} \sim 1.0$) is also observed in [32] for three-dimensional laminar flow simulations.

A snapshot of the vortex shedding pattern and the deforming mesh is displayed in Fig. 16. The iso-surfaces of the span wise vorticity follow the curvature of the cylinder. The deformation of the general hybrid mesh is clear especially at the right end where the sliding boundary condition is applied.

7. Conclusions

A geometrically conservative finite-volume ALE scheme was presented with a moving mesh source term. The moving mesh source term was derived from the physical conservation laws for an arbitrarily moving control volume. Inclusion of the moving mesh source term preserved the uniform flow on arbitrarily deforming meshes. The proposed ALE scheme with moving mesh source has been shown to preserve its formal temporal accuracy which it has on the fixed mesh counterpart.

A strong coupling scheme based on predictor–corrector method was proposed and proved to be more stable compared to the weak coupling approach. Further, it yielded higher temporal accuracy than its weakly-coupled counterpart. Finally, the strongly coupled scheme required fewer iterations of the corrector step.

The presented ALE scheme was applied to the fluid–structure interaction problem involving vortex-induced vibrations of a cylinder in two and three dimensions. The developed scheme was employed with hybrid meshes consisting of four different types of elements (prisms, hexahedra, tetrahedra and pyramids) and yielded good agreement with different computational and experimental results. Phase transitions between hydrodynamics force (C_L) and cross-flow vibration amplitude (y) were observed.

Acknowledgement

Support from the Offshore Technology Research Center for the flow simulations is appreciated.

References

[1] C. Hirt, A. Amsden, J.L. Cook, An arbitrary Lagrangian–Eulerian computing method for all flow speeds, Journal of Computational Physics 14 (1974) 227–253.
[2] T. Tezduyar, M. Behr, J. Liou, A new strategy for finite element computations involving moving boundaries and interfaces – The deforming-spatial-domain/space–time procedure: I. The concept and the preliminary numerical tests, Computer Methods in Applied Mechanics and Engineering 94 (1992) 339–351.
[3] T. Tezduyar, M. Behr, S. Mittal, J. Liou, A new strategy for finite element computations involving moving boundaries and interfaces – The deforming-spatial-domain/space–time procedure: II. Computation of free-surface flows, two-liquid flows, and flows with drifting cylinders, Computer Methods in Applied Mechanics and Engineering 94 (1992) 353–371.
[4] C. Peskin, Numerical analysis of blood flow in the heart, Journal of Computational Physics 25 (1977) 220–252.
[5] C.S. Peskin, The immersed boundary method, Acta Numerica 11 (2002) 479–517.
[6] L.T. Zhang, A. Gerstenberger, X. Wang, W.K. Liu, Immersed finite element method, Computer Methods in Applied Mechanics and Engineering 193 (2004) 2051–2067.
[7] R. Loubère, M.J. Shashkov, A subcell remapping method on staggered polygonal grids for arbitrary-Lagrangian–Eulerian methods, Journal of Computational Physics 209 (2005) 105–138.
[8] J.C. Campbell, M.J. Shashkov, A tensor artificial viscosity using a mimetic finite difference algorithm, Journal of Computational Physics 172 (2001) 739–765.
[9] T.J.R. Hughes, W.K. Liu, T.K. Zimmerman, Lagrangian–Eulerian finite element formulation for incompressible viscous flows, Computer Methods in Applied Mechanics and Engineering 29 (1981) 329–349.
[10] T. Nomura, T.J.R. Hughes, An arbitrary Lagrangian–Eulerian finite element method for interaction of fluid and a rigid body, Computer Methods in Applied Mechanics and Engineering 95 (1992) 115–138.

[11] J. Donea, S. Giuliani, J.P. Halleux, An arbitrary Lagrangian–Eulerian finite element method for transient dynamic fluid–structure interactions, Computer Methods in Applied Mechanics and Engineering 33 (1982) 689–723.
[12] M. Lesoinne, C. Farhat, Geometric conservation laws for flow problems with moving boundaries and deformable meshes, and their impact on aeroelastic computations, Computer Methods in Applied Mechanics and Engineering 134 (1996) 71–90.
[13] B. Koobus, C. Farhat, Second-order time-accurate and geometrically conservative implicit schemes for flow computations on unstructured dynamic meshes, Computer Methods in Applied Mechanics and Engineering 170 (1999) 103–129.
[14] C. Farhat, P. Geuzaine, C. Grandmont, The discrete geometric conservation law and the nonlinear stability of ale schemes for the solution of flow problems on moving grids, Journal of Computational Physics 174 (2001) 669–694.
[15] C. Farhat, P. Geuzaine, G. Brown, Application of a three-field nonlinear fluid–structure formulation to the prediction of the aeroelastic parameters of an f-16 fighter, Computer & Fluids 32 (2003) 3–29.
[16] P. Geuzaine, C. Grandmont, C. Farhat, Design and analysis of ale schemes with provable second-order time-accuracy for inviscid and viscous flow simulations, Journal of Computational Physics 191 (2003) 106–227.
[17] K.W. Schulz, Y. Kallinderis, Unsteady flow structure interaction for incompressible flows using deformable hybrid grids, Journal of Computational Physics 143 (1998) 569–597.
[18] R. Löhner, Applied CFD Techniques: An Introduction Based on Finite Element Methods, Wiley, New York, 2001.
[19] X. Chen, G. Zha, Z. Hu, Numerical simulation of flow induced vibration based on fully coupled fluid–structural interactions, AIAA Paper 2004-2240.
[20] A.J. Chorin, A numerical method for solving incompressible viscous flow problems, Journal of Computational Physics 2 (1967) 12–26.
[21] A. Belov, A. Jameson, L. Martinelli, A new implicit algorithm with multigrid for unsteady incompressible flow calculations, AIAA Paper 95-0049.
[22] A. Jameson, Time-dependent calculations using with applications to unsteady flows past airfoils and wings, AIAA Paper 91-1596.
[23] P. Thomas, K. Lombard, Conservation law and its application to flow computations on moving grids, AIAA Journal 17 (1979) 1030–1037.
[24] Y. Kallinderis, H.T. Ahn, Incompressible Navier–Stokes method with general hybrid meshes, Journal of Computational Physics 210 (2005) 75–108.
[25] A. Haselbacher, J. Blazek, On the accurate and efficient discretization of the Navier–Stokes equations on mixed grids, AIAA Journal 38 (2000) 2094–2102.
[26] N.D. Melson, M.D. Sanetrik, H.L. Atkins, Time-accurate Navier–Stokes calculations with multigrid acceleration, in: 6th Copper Mountain Conference on Multigrid Methods, 1993, p. 423.
[27] L. Martinelli, Calculation of viscous flows with a multigrid method, Ph.D. Thesis, Princeton University, 1987.
[28] R.C. Swanson, E. Turkel, Multistage schemes with multigrid for Euler and Navier–Stokes equations: components and analysis, Technical Report 3631, NASA, 1997.
[29] H.T. Ahn, A new incompressible Navier–Stokes method with general hybrid meshes and its application to flow/structure interactions, Ph.D. Thesis, The University of Texas at Austin, 2005.
[30] T. Yang, Finite Element Structural Analysis, Prentice-Hall, Englewood Cliffs, NJ, 1986.
[31] D.J. Newman, G.E. Karniadakis, A direct numerical simulation study of flow past a freely vibrating cable, Journal of Fluid Mechanics 344 (1997) 95–136.
[32] C. Evangelinos, G. Karniadakis, Dynamics and flow structures in the turbulent wake of rigid and flexible cylinders subject to vortex-induced vibrations, Journal of Fluid Mechanics 400 (1999) 91–124.
[33] G.P. Guruswamy, Unsteady aerodynamic and aerostatic calculations for wings using Euler equations, AIAA Journal 28 (1990) 461–469.
[34] J.J. Alonso, A. Jameson, Fully-implicit time-marching aeroelastic solutions, AIAA Paper 94-0056.
[35] R.D. Cook, D.S. Malkus, M.E. Plesha, Concepts and Applications of Finite Element Analysis, Wiley, New York, 1989.
[36] O.M. Griffin, Vortex-induced vibrations of marine structures in uniform and sheared currents, Technical Report NSF workshop on Riser Dynamics, University of Michigan, 1992.